Chemical Science

ROYAL SOCIETY OF CHEMISTRY

EDGE ARTICLE

View Article Online
View Journal

Cite this: DOI: 10.1039/d5sc01072a

All publication charges for this article have been paid for by the Royal Society of Chemistry

Targeted recognition, fluorescent tracking and augmented killing of multi-bacterial infections *via* synergizing a magnetic bead-armored phage cocktail with enzyme-activated AIE probes†

Zhenyue Su,[a] Ling-Hong Xiong, *[b] Jing Zhang,[a] Ben Zhong Tang *[c] and Xuewen He *[a]

Accurate identification and elimination of multi-bacterial infections are critical due to their significant threat to human health, the complexity of synergistic pathogenic mechanisms and their pivotal role in accelerating antibiotic resistance. Here, we developed a multiplex phage-based fluorescence assay using encoded magnetic nanobeads and multifunctional alkaline phosphatase (ALP)-activatable aggregation-induced emission (AIE) probes for synchronously sensitive detection and efficient elimination of multiple pathogenic bacteria. Preselected phages were covalently conjugated to magnetic nanobeads to form a phage cocktail recipe, enabling specific and precise separation of target bacteria from mixed samples. The high expression of ALP within bacteria triggers enzymatic cleavage of AIE probes, forming luminescent aggregates for sensitive detection, while quinone methide species generated *in situ* exhibit strong chemodynamic and photodynamic activities for enhanced bacterial killing. By combining the inherent bacteriolytic activity of phages on magnetic nanobeads, a significantly boosted efficacy in killing multi-bacterial infections was achieved. Both *in vitro* and *in vivo* experiments demonstrated that this integrated system enables sensitive identification of multi-bacterial infections and augmented antibacterial efficiency, offering a novel strategy for the real-time, precise diagnosis and treatment of multi-bacterial infections.

Received 11th February 2025
Accepted 14th May 2025

DOI: 10.1039/d5sc01072a

rsc.li/chemical-science

Introduction

Bacterial infections are a significant global health concern, ranging from localized conditions such as skin infections to life-threatening systemic diseases such as sepsis.[1] Multi-bacterial infections, characterized by the simultaneous presence of multiple bacterial species at a single infection site, pose even greater threats than mono-bacterial infections.[2] These infections often exhibit increased virulence and resistance to treatment due to synergistic interactions among the pathogens. Unlike simpler infections, multi-bacterial infections involve complex cooperative mechanisms, including enhanced biofilm formation, evasion of immune responses and horizontal transfer of antibiotic resistance genes.[3–5] These factors lead to severe clinical complications such as chronic inflammation, implant-associated infections, sepsis and organ dysfunction, often with higher mortality rates that would impose significant physical and financial burdens on patients and healthcare systems.[3] For example, polymicrobial wound infections involving Gram-positive bacteria such as *Staphylococcus aureus* and Gram-negative bacteria such as *Escherichia coli* not only delay wound healing but also elevate the risk of systemic complications.[6] As the prevalence of multi-bacterial infections continues to increase, there is a pressing demand for advanced diagnostic and therapeutic strategies to address this growing public health challenge.

Most clinical diagnostic techniques rely on selective culturing, which demands large sample volumes, involves time-intensive cultivation and identification processes and often takes several days to yield results.[7] Alternatively, polymerase chain reaction (PCR) techniques, known for their high sensitivity, have been widely employed in diagnostics.[8,9] However, PCR analysis systems are often time-consuming and labor-intensive, and they cannot facilitate real-time monitoring of the infection process involving live bacteria. Recently, advanced

[a]State Key Laboratory of Bioinspired Interfacial Materials Science, The Key Lab of Health Chemistry and Molecular Diagnosis of Suzhou, College of Chemistry, Chemical Engineering and Materials Science, Soochow University, Suzhou 215123, China. E-mail: xheao@suda.edu.cn

[b]School of Public Health, Suzhou Medical College of Soochow University, Soochow University, Suzhou 215123, China. E-mail: xionglinghong@suda.edu.cn

[c]School of Science and Engineering, Guangdong Basic Research Center of Excellence for Aggregate Science, Shenzhen Institute of Aggregate Science and Technology, The Chinese University of Hong Kong, Shenzhen (CUHK-Shenzhen), Guangdong 518172, China. E-mail: tangbenz@cuhk.edu.cn

† Electronic supplementary information (ESI) available. See DOI: https://doi.org/10.1039/d5sc01072a

methods for detecting multiple bacterial species have been developed, including lateral flow assays,[10,11] nanoarray-based biosensors,[12,13] microfluidic systems[14] and aptamer-based fluorescence (FL) assays,[15,16] *etc*. These innovations have significantly improved the simultaneous detection of multiple bacteria. However, they rarely address the simultaneous elimination of the detected bacteria. Antibiotics, as broad-spectrum antimicrobial agents, often lack specificity and require higher dosages to combat multi-bacterial infections, which exacerbates the development of antibiotic resistance.[17,18] To overcome this limitation, antimicrobial peptides have emerged as promising alternatives due to their broad-spectrum activity and low risk of resistance development.[19,20] However, their clinical application is hindered by poor stability against enzymatic degradation and a narrow therapeutic window.[20] In recent years, antimicrobial materials leveraging photothermal and photodynamic (PDT) therapies have gained increasing attention for their localized bacterial killing capabilities.[21–23] By generating heat or reactive oxygen species (ROS) upon light irradiation, these materials provide a low risk of resistance development and effectiveness against biofilm-associated bacteria. Nonetheless, their limitations include shallow light penetration in biological tissues, potential phototoxicity to surrounding healthy cells, and the requirement for precise light delivery. As an antibacterial agent derived from living organisms, phage therapy has emerged as an innovative strategy due to its intrinsic specificity and lytic capabilities against host bacteria with negligible side effects.[24,25] Engineered phages, modified with photodynamic agents on their surfaces, have been developed to achieve targeted bacterial killing with improved efficiency.[26–28] While these engineered phages have shown promising results in the synergistic treatment of single bacterial species, reports on their potential for simultaneously targeting and eliminating multiple bacterial species remain rare. Therefore, there is an urgent need to develop an integrated analysis–killing strategy that combines highly specific and sensitive detection with synergistic and efficient bactericidal activity to address multi-bacterial infections.

Magnetic nanobeads (MNs) offer significant advantages in bioanalyte assays by using a magnetic field,[29] making them ideal for facilely and efficiently isolating and enriching target bacteria from complex samples in both research and clinical settings. However, the specific recognition and binding of target bacteria is the prerequisite for the functioning of magnetic beads in multi-bacterial infections. As a unique fluorophore, aggregation-induced emission luminogens (AIEgens) that exhibit intensified fluorescence after aggregation can be applied in highly sensitive imaging and detection.[30–36] Additionally, after strategic molecular engineering to incorporate photothermal and photodynamic activities, AIEgens can also perform exceptionally in microbial inactivation.[33,34] However, the bacteria-specific enzyme-activatable AIE probe that can synchronously illuminate and eliminate the bacteria is still waiting for exploration.

Herein, we present an integrated strategy combining a magnetic bead-armored phage cocktail and bacterial enzyme-activatable AIE probes for simultaneously detecting and synergistically eliminating multi-bacterial infections. By selecting bacteriophages that specifically target four different bacterial species, we covalently conjugated these phages onto the surface of magnetic beads, enabling the targeted capture, enrichment and separation of various bacteria. Furthermore, alkaline phosphatase (ALP), naturally expressed within the bacteria, catalyzes the hydrolysis of an ALP-activatable multifunctional AIE probe, named TPE-APP, generating strong luminescent photosensitizers and chemodynamic (CDT) active intermediates. Thus, the target bacteria can be not only fluorescently lit up for highly sensitive detection of multi-bacterial infections but also efficiently eliminated *in situ* with the generation of robust ROS through PDT and CDT activities. Combined with the natural bacteriolytic ability of the phages, this integrated detection and killing system provides an effective strategy for identifying and treating multi-bacterial infections.

Results and discussion

Armored phage cocktail system for bacterial recognition and capture

Bacteriophages targeting *S. aureus* (SA), *S. xylosus* (SX), *S. enterica* (SE) and *E. coli* (EC) were obtained through iterative screening. These phages were subsequently conjugated to magnetic beads (MNs) *via* covalent bonding of amino groups with the carboxyl groups on the bead surfaces, forming magnetic bead–phage (MNs@phage) complexes. These complexes leverage the natural targeting capabilities of the phages, achieving high specificity in capturing target bacteria (Scheme 1). In our previous study,[31] we demonstrated that ALP enzymatically hydrolyzes the phosphate group of TPE-APP, producing strongly emissive TPE-DMA aggregates and highly reactive quinone methide (QM) species. These products exhibit potent PDT and CDT effects. Excitingly, ALP, widely expressed in most bacteria,[37,38] can interact with TPE-APP probes, leading to the formation of luminescent TPE-DMA aggregates and QM-active species within bacteria. By combining MNs@phage for the specific capture of diverse target bacteria with the intracellular ALP-specific response of TPE-APP, this approach enables highly sensitive detection and efficient synergistic elimination of multiple bacterial infections (Scheme 1).

MNs@phage offers a superior alternative to immunomagnetic separation for bacterial recognition and isolation.[39] To achieve specific recognition of different bacterial species, four bacteriophages (SA phage, SX phage, SE phage and EC phage) were screened and purified. The morphologies of these phages were investigated by negative-stained transmission electron microscopy (TEM), clearly displaying their head and tail structures (Fig. 1a). The successful conjugation of MNs with bacteriophages is evidenced by the increased hydrated particle size and the changes in zeta potential observed before and after MN modification (Fig. S1†). Furthermore, nucleic acid staining (GelRed) results for MNs and MNs@phage further confirm the effective immobilization of bacteriophages on the bead surface (Fig. S2†). The conjugation efficiencies of MNs@SA phage, MNs@SX phage, MNs@SE phage and MNs@SX phage were

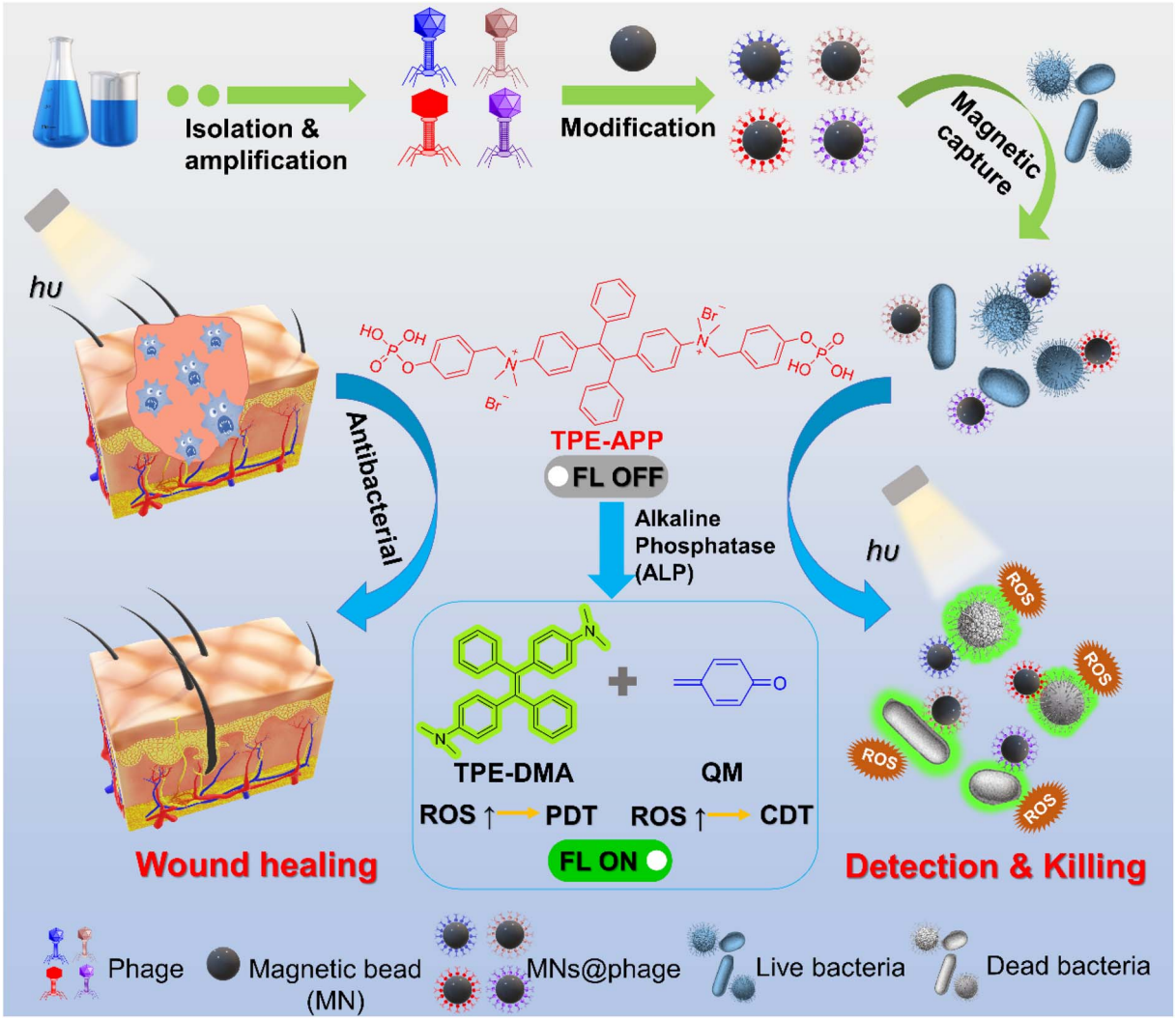

Scheme 1 Targeted recognition and synergistic killing of multiple bacterial infections *via* armored phage cocktails. Magnetic beads modified with phages enable targeted recognition of multiple bacterial strains and highly sensitive detection of these bacteria. This detection is based on the bacterial alkaline phosphatase-activation of AIE probes, leading to the generation of TPE-DMA and QM, which contribute to synergistic bacterial elimination in complex infection systems.

impressively high, achieving 93.5%, 94.1%, 93.2% and 94.3%, respectively (Fig. S3†). Additionally, the average number of phages on each MN was estimated by plaque assay, yielding approximately 118 SA phages, 123 SX phages, 124 SE phages, and 168 EC phages per MN, respectively (Fig. 1b and Table S1†). These results demonstrate that the MNs were successfully functionalized with phages.

To further evaluate the ability of MNs@phage to efficiently capture targeted bacteria, colocalization analysis was conducted using confocal microscopy. As shown in Fig. 1c, nearly 100% of the green FL from SE labeled with the nucleic acid dye DMAO overlapped with the red FL from GelRed-labeled MNs@SE phage. This result indicated that MNs@SE phage successfully achieved simultaneous selective targeting and efficient capture of SE. To further assess whether the modified phage can retain its bactericidal activity, MNs@phage demonstrated the capability to initiate phage infection in targeted bacteria, as confirmed by plaque assays in Fig. S4.† The lytic capability of phages immobilized on the MNs was virtually identical to that of free phages according to the plate culture method (Fig. 1d and S4†). This observation suggested that the conjugation process had no adverse impact on either the targeting efficiency or the ability of the phages to infect and lyse their host bacteria. The specific recognition capability of MNs@phage toward targeted bacteria was also further evaluated. As shown in Fig. 1e, the capture efficiency of MNs@SA phage, MNs@SX phage, MNs@SE phage and MNs@EC phage toward SA, SX, SE and EC, respectively, reached nearly 100%. Negligible nonspecific adsorption was observed when the MNs@phage complexes were co-incubated with non-target bacteria. Moreover, the hydrated particle size of MNs@phage remained nearly unchanged over the course of one month (Fig. S5†), with the recognition and capture efficiency for targeted bacteria consistently exceeding 95% during this period (Fig. 1f). Additionally,

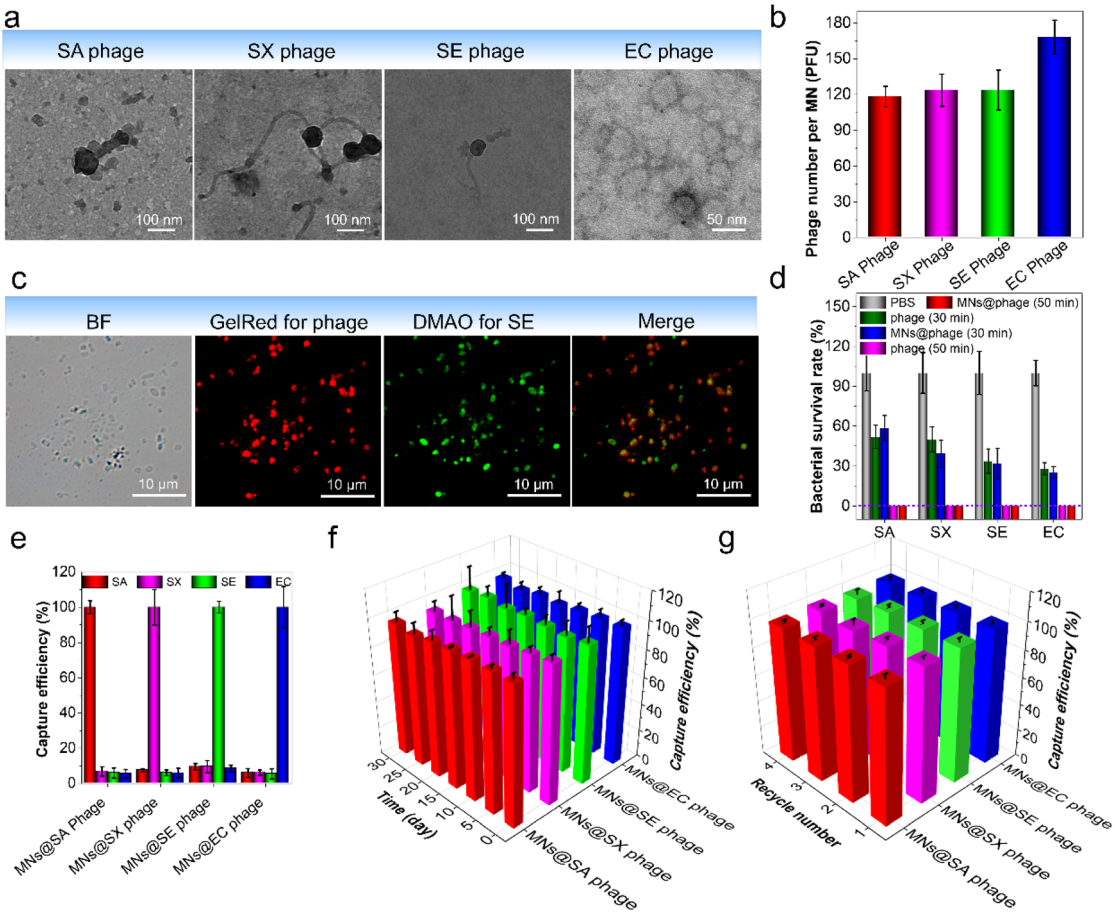

Fig. 1 Characterization of MNs@phage. (a) TEM images of phages targeting *S. aureus* (SA), *S. xylosus* (SX), *S. enterica* (SE) and *E. coli* (EC), respectively. (b) Average number of phages bound to each magnetic nanoparticle (MN). The calculated average phage numbers per MN were 118, 124, 124 and 168 for SA, SX, SE and EC phages, respectively. (c) Bright-field and FL images of MNs@SE phage capturing SE. Red FL represents GelRed-labeled SE phage ($\lambda_{ex} = 365$ nm, $\lambda_{em} = 580-650$ nm), while green FL corresponds to DMAO-labeled SE ($\lambda_{ex} = 488$ nm, $\lambda_{em} = 510-560$ nm). (d) Analysis of the targeting ability and infectivity of phages modified on MNs. (e) The specificity evaluation of MNs@phage for bacterial capture. The concentration of target bacteria was 5×10^6 CFU mL^{-1}, while the concentrations of bacteria in the negative control were 10 times higher than that of the target bacteria. (f) Stability of MNs@phage for bacterial recognition and capture after 30 days of storage. (g) Reusability test of MNs@phage for bacterial recognition and capture.

MNs@phage demonstrated the capability for repeated bacterial capture, retaining a recognition and capture efficiency above 95% even after four consecutive cycles (Fig. 1g). These findings highlight the excellent stability and reliable specificity of MNs@phage in bacterial targeting, underscoring its practical applicability in high-sensitivity bacterial detection.

Specific and sensitive assay of multiple bacteria

In our previous report, the TPE-APP probe was shown to be selectively hydrolyzed by ALP, forming strong emissive TPE-DMA aggregates with typical AIE properties (Fig. S6 and S7†).[31] Since ALP is widely expressed in most bacteria, the TPE-APP probe can leverage this characteristic to achieve a highly sensitive response to intracellular ALP, enabling bacterial illumination as a FL signal output for detection. As expected, when the TPE-APP probes were incubated with four different bacterial species, a gradual increase in FL intensity was observed over time (Fig. 2a, b and S8†). This phenomenon was primarily due to the water-soluble TPE-APP probes entering the bacterial cells, where it was hydrolyzed by intracellular ALP to form fluorescent TPE-DMA, thereby lighting up the bacteria. Conversely, when the bacteria were pretreated with sodium vanadate (Na_3VO_4) prior to incubation with TPE-APP, FL emission within the bacterial cells was significantly reduced or completely absent (Fig. 2a, c and S8†). This inhibition occurred because sodium vanadate suppresses the activity of intracellular ALP, thereby hindering the enzymatic hydrolysis of TPE-APP probes. These results further validated the specific response of TPE-APP to bacterial intracellular ALP. Moreover, the four different bacterial species exhibited significant differences in FL intensity in response to 120 μM TPE-APP. The FL intensity emitted from the bacteria was in the order of SA > SX > SE > EC (Fig. 2d), which attributed to the varying levels of ALP expression among these bacterial species. Specifically, intracellular ALP measurements revealed that SA exhibited the highest ALP expression, followed by SX, SE and the lowest expression in EC (Fig. 2e), aligning with the FL intensity generated by intracellular hydrolysis.

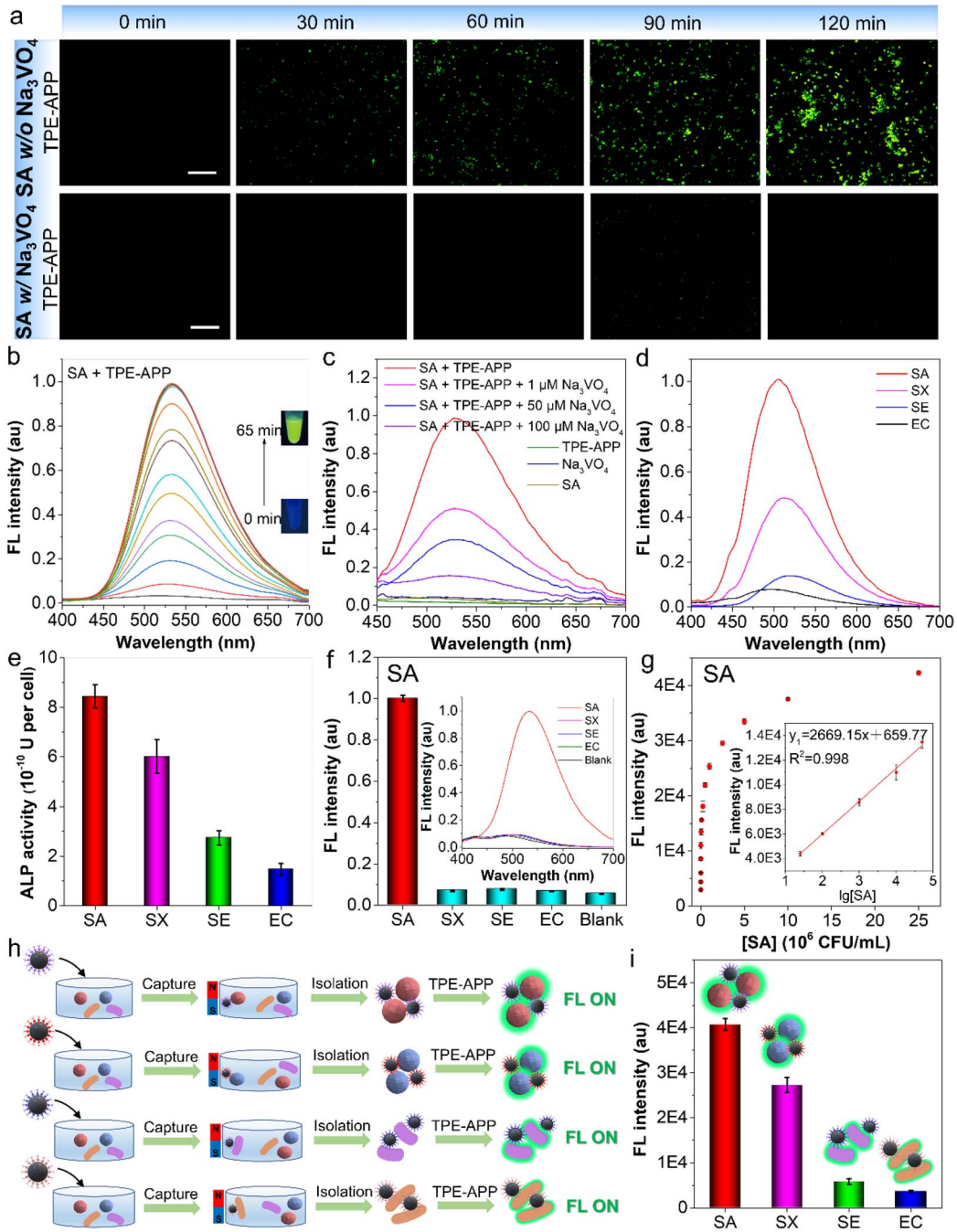

Fig. 2 MNs@phage for target bacterial capture and intracellular ALP response toward the TPE-APP probe for multiple bacterial detection. (a) FL imaging of SA (5×10^7 CFU mL^{-1}) without (w/o) sodium orthovanadate (Na_3VO_4) for 60 min, SA with (w/) Na_3VO_4 (100 μM) for 60 min, followed by incubation with TPE-APP (120 μM) for 0, 30, 60, 90 and 120 min. Scale bar: 10 μm. (b) FL spectra of SA (1×10^8 CFU mL^{-1}) incubated with TPE-APP (120 μM) at different time points. (c) FL spectra of SA in the presence and absence of the TPE-APP probe or Na_3VO_4. (d) FL spectra of SA, SX, SE and EC (5×10^7 CFU mL^{-1}) incubated with TPE-APP probes (120 μM) for 2 h, respectively. (e) Monitoring ALP activities in SA, SX, SE and EC. (f) Specificity analysis of the assay for SA detection. The concentration of bacteria was 5×10^6 CFU mL^{-1}, while the concentrations of the negative control bacteria were 10 times higher than that of the target bacteria. (g) Sensitivity analysis of the assay for SA detection. FL intensity is plotted against SA concentration, with the linear detection range shown in the inset. (h) Schematic illustration of the detection process for four types of bacteria. (i) Detection of four types of bacteria in mixed bacterial samples.

Building on the turn-on FL signal after the TPE-APP response to bacterial cells, MNs@phage was integrated into the detection system to capture the target bacteria, facilitating highly sensitive detection of various bacterial species. After optimization, the ideal conditions for MNs@phage to achieve the highest bacterial capture efficiency were determined to be a concentration of 0.15 mg mL^{-1} and an incubation time of 40 min (Fig. S9 and S10†). The excellent selectivity of the FL assay

was confirmed by testing SA, SX, SE, EC and PBS buffer. Strong FL signals were observed only in the presence of *S. aureus*, while no obvious FL appearing in the negative samples (Fig. 2f). Because the negative samples cannot be recognized and captured by MNs@SA phage, and after washing off, there was no ALP present to hydrolyze TPE-APP to form the FL TPE-DMA aggregates. Similarly, the detection of SX, SE, and EC also exhibited outstanding specificity, consistent with the detection of SA (Fig. S11†). To evaluate the sensitivity and linear analytical range of the FL assay, various concentrations of targeted bacteria were tested. MNs@SA phage was first utilized for SA capture. After magnetic isolation and washing, TPE-APP was added to the MNs@SA phage@SA complex for further incubation. As shown in Fig. 2g, an increased SA concentration caused a proportional increase in the amount of hydrolyzed TPE-APP, resulting in a significant enhancement in the FL intensity of the hydrolyzed product TPE-DMA. The FL intensity at 525 nm of TPE-DMA exhibited a linear increase in the range of 25 to 5×10^4 CFU mL^{-1}, with a limit of detection (LOD) as low as 10.0 CFU mL^{-1}. Furthermore, by applying the same analytical method, the LODs for SX, SE and EC were determined to be 13.1, 24.5 and 1.0×10^4 CFU mL^{-1} (Fig. S12†), respectively.

Leveraging the exceptional capture and enrichment capabilities of MNs@phage for targeted bacteria, this analytical method was further extended to enable the simultaneous detection of multiple bacterial species. A multi-bacterial sample was prepared by mixing four bacterial species at equal concentrations (5×10^7 CFU mL^{-1}). Four types of MNs@phage, each specific to a target bacterium and used at the same concentration (0.15 mg mL^{-1} according to the amounts of MNs), were employed to selectively capture the target bacteria from the mixture. Following incubation with the TPE-APP probe, successful simultaneous detection of all four bacterial species was achieved as the output observable FL signals (Fig. 2g). As shown in Fig. 2h, the FL intensity for each detection correlated positively with the intracellular enzyme expression levels of the respective bacteria.

Synergized CDT–PDT inactivation of target bacteria

The response of the TPE-APP probe toward the intracellular enzyme generated TPE-DMA, which not only exhibited strong FL but also functioned as a photosensitizer for robust ROS generation. As depicted in Fig. S13a,† the presence of TPE-DMA under white-light irradiation (5 mW cm^{-2}) led to a steady increase in the emission intensity of DCFH, reaching nearly a 30-fold enhancement within 5 min. Additionally, another active product, QM, possessed excellent chemodynamic activity as verified in our previous work.[31] In the mixture of TPE-APP, ALP and DCFH, the emission intensity of DCFH gradually increased over time in the dark, reaching nearly a 9.5-fold enhancement within the same time frame (Fig. S13b†). To identify the types of ROS generated, electron spin resonance (ESR) analysis was conducted. 2,2,6,6-Tetramethylpiperidine (TEMP) was used as a spin-trapping agent for $^1O_2$. Upon white light irradiation, the activated TPE-APP probes exhibited a distinct ESR signal characterized by a typical 1 : 1 : 1 triplet pattern in the range of 323–329 mT (Fig. S14b†), confirming the generation of $^1O_2$. In addition, characteristic peaks corresponding to hydroxyl radicals (·OH) were detected in the ESR spectra using 5,5-dimethyl-1-pyrroline *N*-oxide (DMPO) as the spin-trapping agent in the dark (Fig. S14a†). These results indicate that the primary ROS generated by activated TPE-APP probes is $^1O_2$ *via* photodynamic activity, followed by ·OH production through chemodynamic activity. Consequently, this approach enabled simultaneous bacterial detection and a synergistic CDT–PDT antibacterial effect.

The CDT and PDT antibacterial performances of TPE-APP probes upon the intracellular enzymatic hydrolysis were subsequently evaluated, given their exceptional efficiency in generating ROS. *N*,*N*-Dimethylaniline *N*-oxide (DMAO) was used for live/dead bacterial staining, while propidium iodide (PI) was employed to stain dead bacteria, assessing the antibacterial efficacy of TPE-APP probes. When SA was treated with TPE-APP in the dark, partial bacterial death was observed, as evidenced by the emitted red FL signal. Following 40 min of white-light irradiation, bacterial mortality rates exceeded 90%, as indicated by the red-colored PI staining (Fig. 3a). For quantitative evaluation, the CDT and PDT inactivation activities of TPE-APP probes toward SA, SX, SE and EC were assessed by the plate colony counting method (Fig. 3b). TPE-APP showed dose-independent antibacterial activity in various bacteria in the dark, which was attributed to the CDT activity from the QM product. In addition, bactericidal efficacies of TPE-APP probes were significantly enhanced under white light irradiation due to the combination of PDT and CDT activities. Due to the differences in ALP expression levels among the four bacterial species, the amount of TPE-APP hydrolysis products also varied. As a result, under identical conditions of TPE-APP probe concentration and bacterial count, the antibacterial efficiency exhibited corresponding differences. As shown in Fig. 3b, when subjected to 40 min of white light irradiation, a 100% bacterial killing efficiency of TPE-APP (120 μM) toward SA was achieved. However, under the same conditions, the bactericidal efficacies toward SX, SE and EC were 81.5%, 66.9%, 60.0%, respectively. Increasing the concentration of TPE-APP or extending the light irradiation time can also achieve higher killing efficiency against SX, SE and EC (Fig. 3b and S15†). We further employed scanning electron microscopy (SEM) to investigate the bacterial morphological alterations before and after TPE-APP treatments. As shown in Fig. 3c, the white light irradiation alone caused no observable damage to the bacterial cell membranes. In contrast, under both dark and light irradiation conditions, the bacterial membranes of SA, SX, SE and EC incubation with TPE-APP probes exhibited significant damage, with numerous pores and wrinkles forming on the membrane surfaces, ultimately leading to noticeable disintegration of bacterial structures. Bacterial membrane damage was significantly more severe under light irradiation compared to dark conditions, primarily due to the synergistically enhanced antibacterial effects of CDT and PDT.

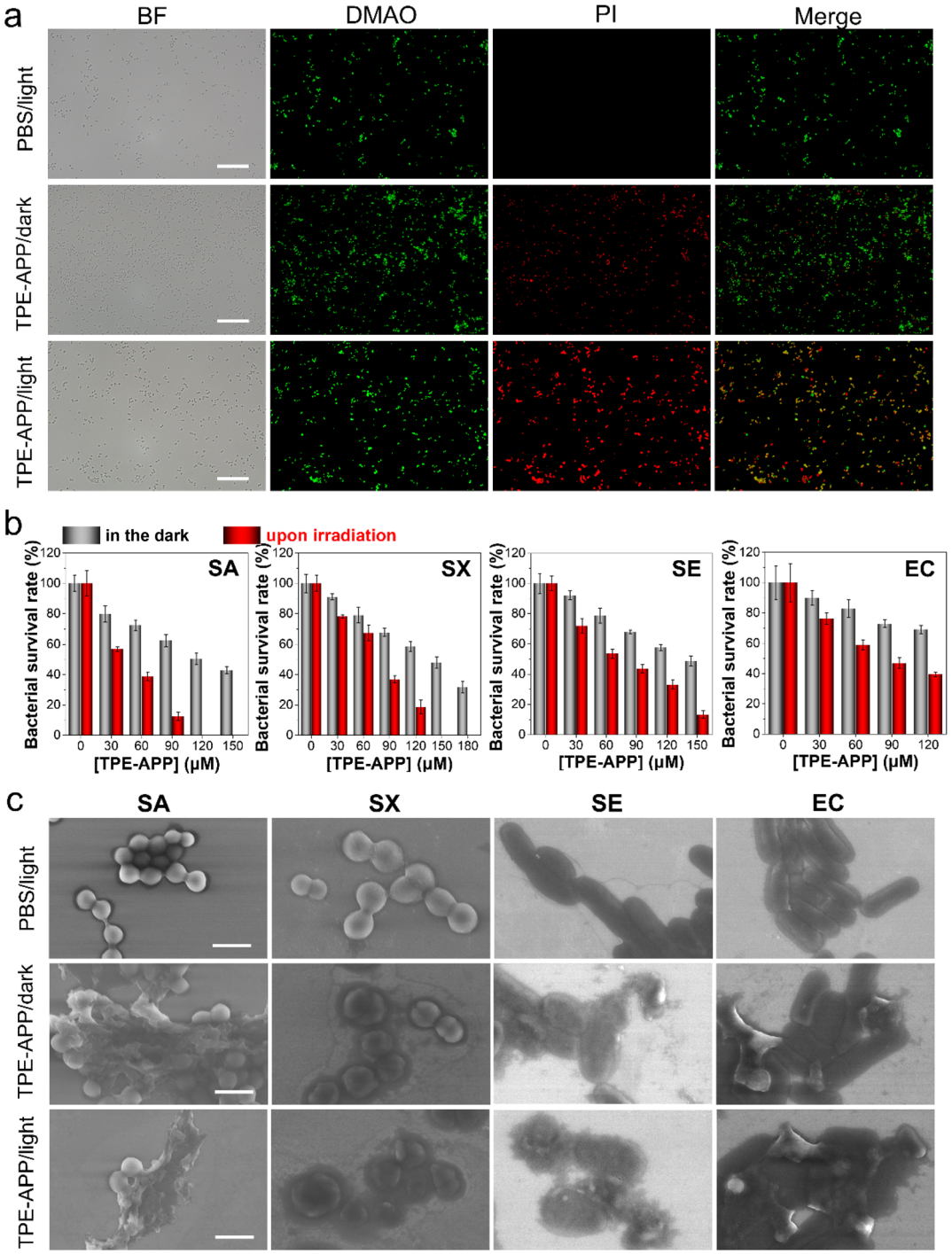

Fig. 3 Bactericidal capability of TPE-APP probes. (a) DMAO/PI staining to differentiate total (green) and dead bacteria (red) SA bacteria (1.0×10^7 CFU mL^{-1}) after incubation with the TPE-APP probe (130 μM) for 2 h, followed by either dark conditions or white light irradiation (40 min, 5 mW cm^{-2}). Scale bars: 10 μm. (b) Calculated survival rates of SA, SX, SE and EC after treatment with various TPE-APP probes under dark conditions or white light irradiation (5 mW cm^{-2}) for 40 min, respectively. (c) SEM images of SA, SX, SE and EC following different treatments under dark conditions or white light irradiation for 30 min. Scale bars: 1.5 μm.

Antibacterial mechanism investigation and biofilm killing

To further explore the underlying antibacterial mechanism of TPE-APP, intracellular ROS levels in four different bacterial species were monitored by using DCFH-DA as an indicator. Upon white-light irradiation, distinct green FL was observed in four different bacterial species treated with TPE-APP and DCFH-DA (Fig. 4a). The FL intensity was significantly stronger than that observed under dark conditions, while no detectable FL signal was observed in the absence of TPE-APP. The superior ROS generation capability of TPE-APP hydrolysis by intracellular

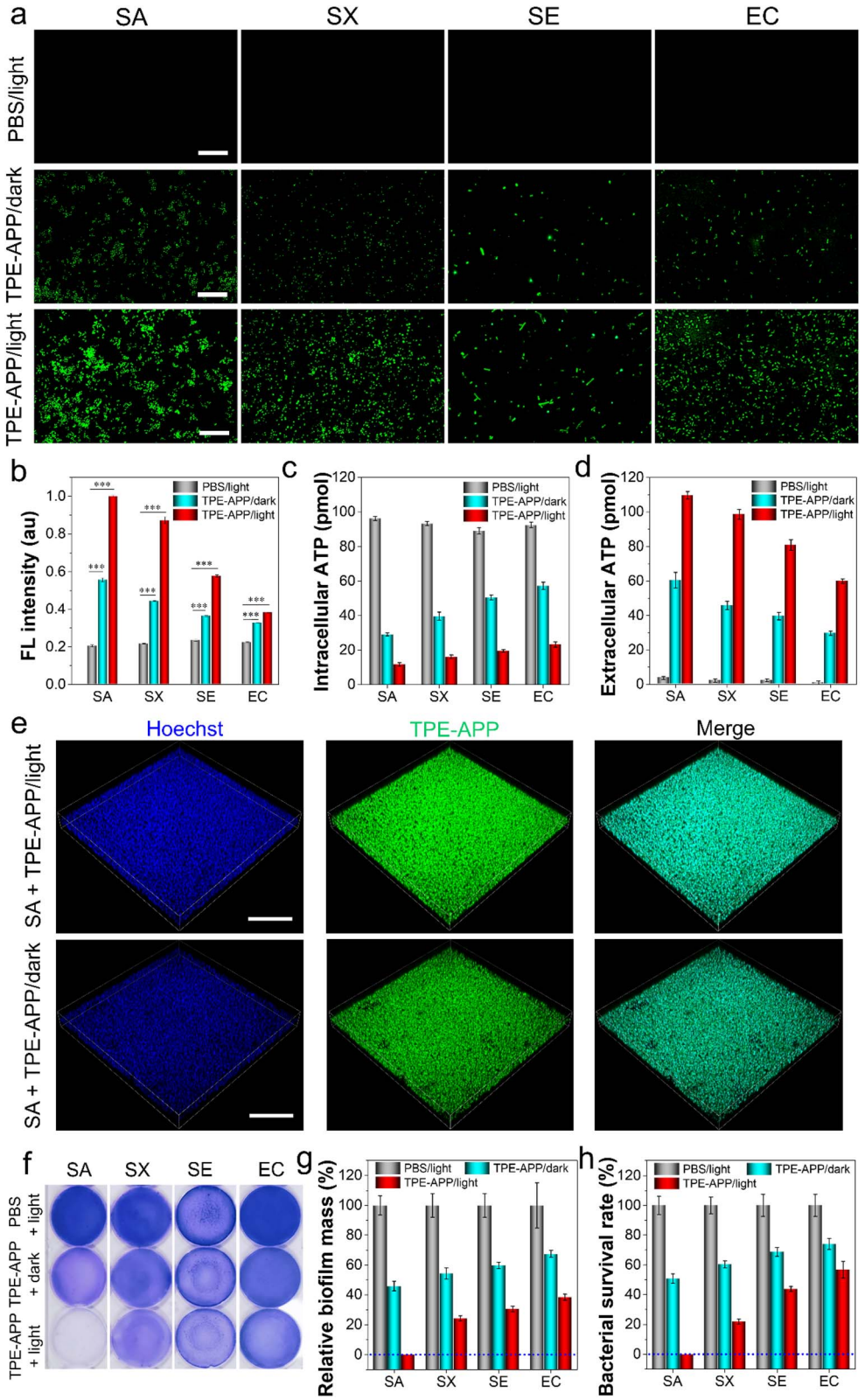

Fig. 4 Bacterial killing by TPE-APP probes through ROS caused cell membrane damage. (a) ROS generation in SA, SX, SE and EC (5×10^7 CFU mL^{-1}) after treatment with TPE-APP (120 μM) for 2 h, followed by either dark conditions or white light irradiation (30 min, 5 mW cm^{-2}), measured using DCFH-DA (10 μM) as an indicator. Scale bar: 10 μm. (b) Membrane potential changes in SA, SX, SE and EC treated with TPE-APP probes under different conditions. ***$P < 0.001$. (c and d) Extracellular and intracellular ATP levels of different bacteria treated with 120 μM TPE-APP for 2 h, followed by either dark conditions or white light irradiation (40 min, 5 mW cm^{-2}). (e) Biofilm imaging after treatment with TPE-APP under dark conditions or white light irradiation (5 mW cm^{-2}) for 60 min. Blue color represents Hoechst for nucleus staining ($\lambda_{ex} = 405$ nm, $\lambda_{em} = 430-475$ nm), and green color represents TPE-DMA ($\lambda_{ex} = 405$ nm, $\lambda_{em} = 500-550$ nm). Scale bar: 500 μm. (f) Crystal violet staining of biofilms formed by

ALP was largely attributed to the synergistic effect of ROS generation induced by TPE-DMA and QM. These intracellular ROS were likely to disrupt the bacterial membrane structure (Fig. 3c), eventually leading to bacterial death. Furthermore, the antibacterial efficacy can be linked to a membrane disruption mechanism.

Bacteria also rely on their membrane potential for signaling and information processing.[40] Membrane rupture results in depolarization of the bacterial membrane potential, which can be detected using the fluorescent probe 3,3′-dipropylthiadicarbocyanine iodide (DiSC3(5)) as an indicator. As shown in Fig. 4b, significant FL intensity enhancements were observed in bacteria treated with TPE-APP compared to the untreated control group, under both dark conditions and following white light irradiation (5 mW cm^{-2}) for 40 min. The light-irradiated group exhibited a markedly greater increase in FL intensity than the dark group, further demonstrating that the killing effect of activated TPE-APP probes on these bacteria was significantly enhanced by generation of CDT and PDT products after the ALP response.

Additionally, membrane damage affected intracellular adenosine triphosphate (ATP) levels, causing substantial ATP leakage into the extracellular environment. To assess this, intracellular ATP and extracellular ATP in the supernatant were measured after bacterial cell treatment with TPE-APP probes. As depicted in Fig. 4c, a marked reduction in intracellular ATP content was observed across all four bacterial species treated with TPE-APP compared to the untreated bacteria, confirming effective ATP release. Conversely, the extracellular ATP contents in the bacterial supernatant were significantly elevated in the TPE-APP-treated group compared to the untreated control group (Fig. 4d). Moreover, with the same number of bacteria, the DNA content in the culture supernatant also increased in the TPE-APP-treated group, while no discernible DNA bands were detected in the control groups (Fig. S16†). These findings further clarified that the cell wall and membrane damage caused by activated TPE-APP within bacteria resulted in the leakage of ATP, DNA and other intracellular components from SA, SX, SE and EC. Collectively, these results underscore the conclusion that bacterial killing was achieved through the synergistic effects of CDT and PDT activities.

As reported, bacterial infections are often accompanied by the formation of bacterial biofilms, which exhibit significantly higher resistance to active drugs and antibiotics compared to planktonic bacteria.[41] To address this challenge, the biofilm elimination capability of TPE-APP probes was investigated through imaging analysis and crystal violet assays. The SA biofilm structure was first analyzed using confocal microscopy. As shown in Fig. 4e, the FL intensity of the probe-treated group under light conditions was significantly higher than that under dark conditions. This enhancement can be attributed to the synergistic killing effect of the reaction products under light exposure, which disrupted the structural integrity of the bacterial biofilm. This disruption facilitated the penetration of more TPE-APP probes into the biofilm, allowing them to react with intracellular ALP, which was also confirmed by the enhanced ROS generation within the biofilm compared to the dark group (Fig. S17†). Thus, an increased number of TPE-DMA aggregates were generated, resulting in a pronounced enhancement of FL intensity. Furthermore, the biofilm penetration capability and the oxidative stress generated by activated TPE-APP probes were evaluated for their biofilm elimination and bactericidal effects. Crystal violet staining experiments demonstrated that activated probes achieved biofilm biomass removal rates of 100%, 75.8%, 69.4% and 61.7% for SA, SX, SE and EC, respectively, under the same probe concentration and white light irradiation conditions (Fig. 4f and g), which were markedly higher than those observed under dark conditions. The significant differences in biofilm removal efficiency among various bacterial species were primarily due to differences in intracellular ALP expression levels. Higher ALP expression resulted in increased ROS production, leading to more effective bacterial elimination. Furthermore, elevated ALP levels promoted deeper penetration of TPE-APP probes into the biofilm, enabling more extensive disruption of the biofilm structure. The remarkable performance of TPE-APP probes under light irradiation can be ascribed to two aspects: first, the water-soluble TPE-APP effectively penetrated biofilms and interacted with intracellular ALP to produce CDT-activated products and AIE photosensitizers. Second, the activated TPE-APP probes generated a substantial amount of ROS through the synergistic effects of PDT and CDT, promoting efficient biofilm elimination.

Building on the synergistic antibacterial effects of the activated TPE-APP probe, further research was conducted to explore its capability for simultaneous elimination of multiple bacterial populations. When four bacterial species at identical concentrations were mixed and co-incubated with the TPE-APP probe for 2 h, followed by 40 min of white light irradiation, the antibacterial efficacy of TPE-APP against the multiple bacteria was found to strongly correlate with the expression levels of ALP within the bacteria. Under white light irradiation, TPE-APP achieved a 100% killing efficiency against SA in the mixed bacterial population, while the killing efficiencies against SX, SE and EC were 78.2%, 56.2% and 43.3%, respectively (Fig. 4h). This result also highlighted that such an intracellular enzyme-responsive probe was capable of effectively eliminating multiple types of bacteria in mixed infections. It lays a robust foundation for addressing cross-infections in multiple bacterial populations with remarkable efficiency.

We have investigated the CDT and PDT effects of the activated TPE-APP in bacterial elimination. In parallel, the

SA, SX, SE and EC after incubation with TPE-APP (130 μM) for 5 h, followed by either dark conditions or white light irradiation (40 min, 5 mW cm^{-2}), respectively. (g) The corresponding relative bacterial survival rates in biofilms after treatments. (h) Survival rates of the four types of bacteria after treatment with the same concentration of TPE-APP probes (120 μM) for 2 h, followed by either darkness or white light irradiation for 40 min (5 mW cm^{-2}).

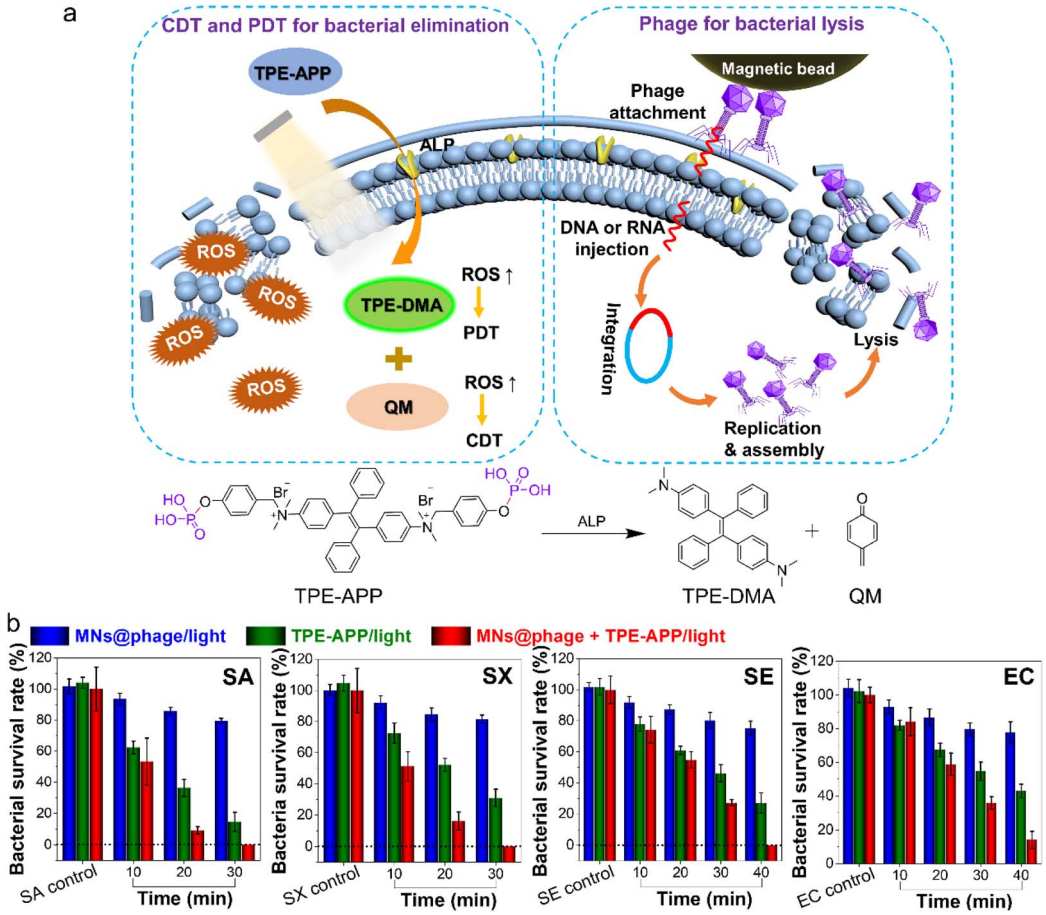

Fig. 5 Synergistic killing of bacterial infections *via* combined CDT/PDT therapy and phage lysis. (a) Schematic illustration depicting the mechanisms of bacterial elimination, including PDT/CDT, phage-induced bacterial lysis and their synergistic effects in combating bacterial infections. (b) Bacterial survival rates of four types of bacteria after various treatments following white light irradiation for different durations.

developed detection and analysis system demonstrated that MNs@phage not only efficiently captured target bacteria but also preserved the bacteriolytic activity of phages immobilized on the magnetic beads. Over extended interaction periods, the phages can deliver nucleic acids into the bacterial cells, leveraging the intracellular environment to assemble new phage particles. These progeny phages were subsequently released, leading to bacterial lysis. By combining CDT and PDT effects with phage-mediated bacterial lysis, this strategy achieved a synergistic and tri-modal approach in bacterial elimination (Fig. 5a). As shown in Fig. 5b, when MNs@phage was incubated with bacteria alone, bacterial viability gradually decreased with prolonged incubation time. During 40 min of incubation, overall bacterial viability remained above 80%, indicating that a certain concentration of phage was capable of partially lysing the bacteria. Similarly, when TPE-APP was incubated with bacteria alone, intracellular ROS production increased with extended light exposure, resulting in progressively enhanced bacterial killing. Following 30 min of light irradiation, the killing efficiencies against SA, SX, SE and EC were 85.3%, 69%, 53.7% and 45.3%, respectively. When MNs@phage and TPE-APP were applied simultaneously, the synergistic killing effect was significantly superior to that of MNs@phage or TPE-APP alone. After 30 min of light irradiation, the synergistic treatment achieved 100% killing of SA and SX, while the killing efficiencies for SE and EC increased to 72.7% and 64.1%, respectively. Further extending the irradiation time to 40 min resulted in 100% killing of SE, with the bacterial survival rate of EC further reduced to just 14.1%. These findings highlighted that the tri-modal synergistic approach achieved significantly enhanced bacterial killing efficiency.

In vivo multiple bacterial elimination and accelerated wound healing

Due to the excellent bactericidal effects observed at the cellular level, we further investigated whether the combination of TPE-APP probes and phages can expedite wound healing and prevent complications in bacteria-infected mouse models. The *in vivo* biosafety of the "phage + TPE-APP/light" treatment was evaluated through routine blood tests and blood biochemistry analysis. As shown in Fig. S18a,† compared to the PBS control group, no significant body weight loss was observed in healthy mice following intraperitoneal injection of "phage + TPE-APP" combined with whole-body white-light irradiation. Moreover, blood cell counts showed no notable differences between the

treatment and control groups (Fig. S18b and c†). Key biochemical indicators, including alanine transaminase (ALT), aspartate aminotransferase (AST), albumin (ALB), blood urea nitrogen (BUN), and creatinine (CRE), remained stable across all treatment groups (Fig. S18d–h†), suggesting that liver and kidney functions were not adversely affected. Histological analysis by hematoxylin and eosin (H&E) staining of major organs, including the heart, liver, spleen, lung, and kidney, on day 10 post-injection revealed no observable pathological abnormalities (Fig. S19†). These results collectively confirm the favorable biocompatibility of "phage + TPE-APP".

Given the excellent biocompatibility of "phage + TPE-APP", *in vivo* antibacterial tests were conducted using subcutaneous abscess models established through local inoculation of SA, SX, SE and EC (Fig. 6a). Once bacterial infections were established, various treatments were applied to the wounds, and the wound recovery of mice in each group was monitored over time. PBS with light irradiation served as the negative control, while the commercial antibiotic methicillin with light served as the positive control. The experimental groups included four types of phages under light irradiation, TPE-APP in darkness, TPE-APP under light irradiation and a combination of phage and TPE-APP under light irradiation. Photographs of the wounds on days −1, 1, 2, 3, 5, 7 and 9 are shown in Fig. 6b. The TPE-APP/light group demonstrated a significantly accelerated healing rate compared to the TPE-APP/dark group, the phage/light group, the antibiotic/light group and the PBS/light group. By day 9, the wound healing rate for the TPE-APP/light group reached 93.8%,

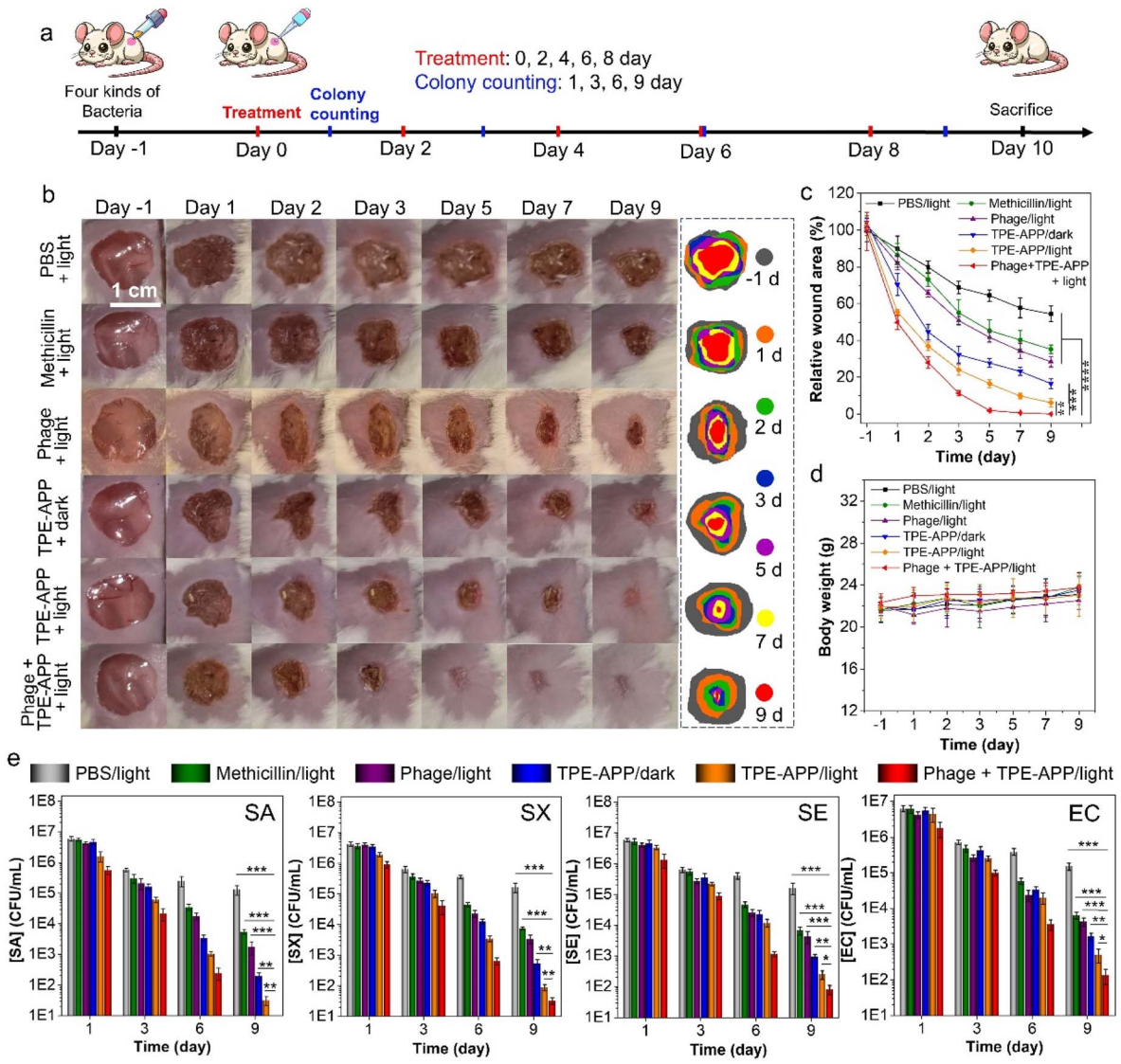

Fig. 6 Targeted recognition and synergistic killing of multiple bacteria in a complex mouse wound model. (a) Schematic diagram illustrating the treatment of multiple bacteria-infected wounds in mice. (b) Photographs showing wound healing in mice after different treatments. Scale bar: 1 cm. (c) Analysis of relative wound size after mixed bacterial infections and various treatments over 9 days. $^{**}P < 0.01$, $^{***}P < 0.001$, $^{****}P < 0.0001$. (d) Body weight changes in mice with mixed bacterial infections during the 9-day treatment period. (e) Bacterial loads of SA, SX, SE and EC in wound tissues on days 1, 3, 6 and 9 after treatment. $^{*}P < 0.05$, $^{**}P < 0.01$, $^{***}P < 0.001$.

markedly higher than that of the dark group (83.5%), the phage/light group (71.6%), the antibiotic/light group (64.8%) and the PBS/light group (45.6%). These results highlighted the accelerated wound healing process due to the combined CDT and PDT effects (Fig. 6c). Furthermore, the tri-modal strategy combining phage and TPE-APP under light irradiation achieved the most effective wound healing, with nearly 100% of the wound area healed by day 9. This underscored the bacteriolytic effect of the phage and emphasized the superior efficacy of the tri-modal synergistic bacterial elimination strategy. Additionally, the minimal weight change observed in treated mice compared to the control group highlighted the significant potential of TPE-APP probes for *in vivo* antibacterial applications (Fig. 6d). Moreover, bacterial populations in the multi-bacterial infection wound model can be monitored in real-time. Using the established detection and analysis method, we tracked bacterial changes in the infected wounds throughout the treatment process. It was observed that the bacterial count within the wounds gradually decreased as the treatment progressed, and the bacterial count exhibited a positive correlation with the measured wound area (Fig. 6e). This indicated that the developed detection method was highly applicable and reliable for use in real multi-bacterial infection samples.

Following a 10-day treatment regimen, wound tissues and major organs from infected mice were collected to investigate histological changes, providing additional confirmation of the enhanced wound healing effects achieved through synergistic bacterial elimination. As illustrated in Fig. S20,† H&E staining images revealed a substantial infiltration of inflammatory cells in skin tissue samples treated with PBS and methicillin under light irradiation. In contrast, treatments with the TPE-APP/light group and the combined phage and TPE-APP under light significantly reduced inflammatory cell infiltration. Notably, no significant changes were observed in other major organs, including the heart, liver, spleen, lungs and kidneys, across all treatment groups, further supporting the safety and biocompatibility of these therapeutic approaches.

The presented strategy offers several advantages over conventional bacterial detection techniques. Firstly, the system enables precise recognition of multiple bacterial strains through the use of multiplex phage-encoded magnetic beads, providing high specificity and significantly reducing false positives commonly associated with traditional culture-based methods or broad-spectrum molecular assays. Secondly, the integration of enzyme-activated AIE probes allows for *in situ* bacterial detection with excellent sensitivity and a high signal-to-noise ratio, outperforming conventional fluorophores that often suffer from limited detection sensitivity and aggregation-caused quenching. Thirdly, this platform achieves enhanced antibacterial efficacy by combining the innate bactericidal activity of phages with the enzyme-triggered activation of AIE probes, enabling localized CDT and PDT. Unlike standard antibiotic treatments or non-specific detection platforms, this multifunctional strategy enables not only accurate detection but also effective elimination of pathogens in a targeted, efficient, and visually traceable manner, making it a highly promising approach for managing complex, multi-bacterial infections.

Conclusions

In summary, an integrated strategy capable of simultaneously achieving sensitive and specific detection and synergistic elimination of multi-bacterial infections was developed. By screening four distinct bacteriophages that can specifically target respective bacterial species and covalently conjugating them onto the surface of magnetic nanoparticles, rapid recognition and isolation of the target bacteria were realized. Additionally, multifunctional probes were catalytically hydrolyzed by bacterial ALP enzyme, forming strongly luminescent AIE aggregates for bacterial detection, with detection limits down to 10 CFU mL^{-1} for SA, 13.1 CFU mL^{-1} for SX, 24.5 CFU mL^{-1} for SE and 1.0×10^4 CFU mL^{-1} for EC, respectively. Moreover, the enzymatic cleavage products, TPE-DMA and QM, exhibited both PDT and CDT activities that can generate robust ROS *in situ* to synergistically eliminate bacteria. By further integrating the bacteriolytic action of the phages on the magnetic nanoparticles, augmented efficiency in specific bacterial elimination was achieved. Both *in vivo* and *in vitro* experiments demonstrated the excellent performance of this integrated system in the treatment of multi-bacterial infections.

Ethical statement

All procedures of animal experiments were approved by the Animal Care and Use Committee of Soochow University and complied with all relevant ethical regulations.

Data availability

The datasets supporting this article have been uploaded as part of the ESI.†

Author contributions

L. H. X. and X. H. conceived the original idea for this study. L. H. X. and X. H. designed the experiments. Z. S. performed the experiments. L. H. X. and X. H. supervised the whole process. Z. S., L. H. X., X. H., and B. Z. T. discussed the manuscript. L. H. X. wrote the manuscript, L. H. X., and X. H. revised the manuscript. All the authors participated in data analysis.

Conflicts of interest

There are no conflicts to declare.

Acknowledgements

The authors acknowledge the support of the National Natural Science Foundation of China (22274106), the Program of Suzhou Innovation and Entrepreneurship Leading Talents (ZXL2022513) and startup funds from Soochow University.

Notes and references

1 S. Hernando-Amado, T. M. Coque, F. Baquero and J. L. Martínez, *Nat. Microbiol.*, 2019, **4**, 1432–1442.
2 R. A. Fisher, B. Gollan and S. Helaine, *Nat. Rev. Microbiol.*, 2017, **15**, 453–464.
3 C. R. Arciola, D. Campoccia and L. Montanaro, *Nat. Rev. Microbiol.*, 2018, **16**, 397–409.
4 J. A. Fuhrman, *Nature*, 2009, **459**, 193–199.
5 E. H. Wintermute and P. A. Silver, *Mol. Syst. Biol.*, 2010, **6**, 407.
6 S. Bertesteanu, S. Triaridis, M. Stankovic, V. Lazar, M. C. Chifiriuc, M. Vlad and R. Grigore, *Int. J. Pharm.*, 2014, **463**, 119–126.
7 K. Hsieh, A. S. Patterson, B. S. Ferguson, K. W. Plaxco and H. T. Soh, *Angew. Chem., Int. Ed.*, 2012, **51**, 4896–4900.
8 D. K. Kang, M. M. Ali, K. Zhang, S. S. Huang, E. Peterson, M. A. Digman, E. Gratton and W. Zhao, *Nat. Commun.*, 2014, **5**, 5427.
9 J. W. F. Law, N. S. Ab Mutalib, K. G. Chan and L. H. Lee, *Front. Microbiol.*, 2015, **5**, 770–789.
10 H. Sohrabi, M. R. Majidi, M. Fakhraei, A. Jahanban-Esfahlan, M. Hejazi, F. Oroojalian, B. Baradaran, M. Tohidast, M. Guardia and A. Mokhtarzadeh, *Talanta*, 2022, **243**, 123330.
11 Y. Liu, L. Zhan, Z. Qin, J. Sackrison and J. C. Bischof, *ACS Nano*, 2021, **15**, 3593–3611.
12 Z. Zhang, Y. Sun, Y. Yang, X. Yang, H. Wang, Y. Yun, X. Pan, Z. Lian, A. Kuzmin, E. Ponkratova, J. Mikhailova, Z. Xie, X. Chen, Q. Pan, B. Chen, H. Xie, T. Wu, S. Chen, J. Chi, F. Liu, D. Zuev, M. Su and Y. Song, *Adv. Mater.*, 2023, **35**, 2211363.
13 T. Tian, J. Yi, Y. Liu, B. Li, Y. Liu, L. Qiao, K. Zhang and B. Liu, *Biosens. Bioelectron.*, 2022, **197**, 113778.
14 C. S. Rossi, F. Coulon, S. Ma, Y. S. Zhang and Z. Yang, *Adv. Funct. Mater.*, 2023, **33**, 2212081.
15 S. Wu, N. Duan, Z. Shi, C. Fang and Z. Wang, *Anal. Chem.*, 2014, **86**, 3100–3107.
16 M. Majdinasab, A. Hayat and J. L. Marty, *TrAC, Trends Anal. Chem.*, 2018, **107**, 60–77.
17 J. Davies and D. Davies, *Microbiol. Mol. Biol. Rev.*, 2010, **74**, 417–433.
18 H. K. Allen, J. Donato, H. H. Wang, K. A. Cloud-Hansen, J. Davies and J. Handelsman, *Nat. Rev. Microbiol.*, 2010, **8**, 251–259.
19 R. E. Hancock and H. G. Sahl, *Nat. Biotechnol.*, 2006, **24**, 1551–1557.
20 C. D. Fjell, J. A. Hiss, R. E. W. Hancock and G. Schneider, *Nat. Rev. Drug Discovery*, 2012, **11**, 37–51.
21 Q. Cui, H. Yuan, X. Bao, G. Ma, M. Wu and C. Xing, *ACS Appl. Bio Mater.*, 2020, **3**, 4436–4443.
22 M. Overchuk, R. A. Weersink, B. C. Wilson and G. Zheng, *ACS Nano*, 2023, **17**, 7979–8003.
23 P. P. Kalelkar, M. Riddick and A. J. García, *Nat. Rev. Mater.*, 2022, **7**, 39–54.
24 S. A. Strathdee, G. F. Hatfull, V. K. Mutalik and R. T. Schooley, *Cell*, 2023, **186**, 17–31.
25 D. Olawade, O. Fapohunda, E. Egbon, O. A. Ebiesuwa, S. O. Usman, A. O. Faronbi, S. C. Fidelis, D. Pires, L. Melo, D. V. Boas, S. S. Sillankorva and J. Azeredo, *Curr. Opin. Microbiol.*, 2017, **39**, 48–56.
26 B. Ran, Y. Yuan, W. Xia, M. Li, Q. Yao, Z. Wang, L. Wang, X. Li, Y. Xu and X. Peng, *Chem. Sci.*, 2021, **12**, 1054–1061.
27 X. He, Y. Yang, Y. Guo, S. Lu, Y. Du, J.-J. Li, X. Zhang, N. L. C. Leung, Z. Zhao, G. Niu, S. Yang, Z. Weng, R. T. K. Kwok, J. W. Y. Lam, G. Xie and B. Z. Tang, *J. Am. Chem. Soc.*, 2020, **142**, 3959–3969.
28 J. Zhang, X. He and B. Z. Tang, *ACS Nano*, 2024, **18**, 3199–3213.
29 L.-H. Xiong, R. Cui, Z.-L. Zhang, X. Yu, Z. Xie, Y.-B. Shi and D.-W. Pang, *ACS Nano*, 2014, **8**, 5116–5124.
30 J. Sun and X. He, *Aggregate*, 2022, **3**, e282.
31 L.-H. Xiong, L. Yang, J. Geng, B. Z. Tang and X. He, *ACS Nano*, 2024, **18**, 17837–17851.
32 L.-H. Xiong, J. Wang, F. Yang, B. Z. Tang and X. He, *Anal. Chem.*, 2024, **96**, 9244–9253.
33 M. M. S. Lee, E. Y. Yu, J. H. C. Chau, J. W. Y. Lam, R. T. K. Kwok and B. Z. Tang, *Adv. Mater.*, 2024, 2407707.
34 L.-H. Xiong, P. Hu, J. Zhang, J. Sun, J. Geng, M.-P. Zhuo, B. Z. Tang and X. He, *ACS Nano*, 2025, **19**, 7898–7909.
35 S. Segawa, X. Ou, T. Shen, T. Ryu, Y. Ishii, H. H. Y. Sung, I. D. Williams, R. T. K. Kwok, K. Onda, K. Miyata, X. He, X. Liu and B. Z. Tang, *Aggregate*, 2024, **5**, e499.
36 J. Sun, J. Geng, B. Z. Tang and X. He, *Adv. Funct. Mater.*, 2024, **34**, 2315299.
37 B. Le-Vinh, Z. B. Akkus-Dağdeviren, N.-M. N. Le, I. Nazir and B. Schnürch, *Adv. Ther.*, 2022, **5**, 2100219.
38 M. Sakurai, J. Wasaki, Y. Tomizawa, T. Shinano and M. Osaki, *Soil Sci. Plant Nutr.*, 2008, **54**, 62–71.
39 J. Chen, Y. Zhou, D. Wang, F. He, V. M. Rotello, K. R. Carter, J. J. Watkins and S. R. Nugen, *Lab Chip*, 2015, **15**, 3086–3094.
40 J. M. Benarroch and M. Asally, *Trends Microbiol.*, 2020, **28**, 304–314.
41 Z. Wang, Y. Peng, Y. Zhou, S. Zhang, J. Tan, H. Li, D. He and L. Deng, *Acta Biomater.*, 2022, **137**, 276–289.